Enhanced Temporal-Resolution CEST Imaging for reliable mapping of muscle OXPHOS

Ritambhar Burman[1], Richard S. Finkel[2,3], Kirsten K. Ness[4], Asim Bag[1], Yuxi Pang[1], Puneet Bagga[1]

[1] Department of Radiology, St. Jude Children's Research Hospital, Memphis, TN, USA

[2] Center for Experimental Neurotherapeutics, St Jude Children's Research Hospital, Memphis, Tennessee, USA

[3] Department of Pediatric Medicine, St Jude Children's Research Hospital, Memphis, Tennessee, USA

[4] Department of Epidemiology and Cancer Control, St Jude Children's Research Hospital, Memphis, Tennessee, USA

Corresponding Address: Puneet Bagga, PhD, Department of Radiology, St. Jude Children's Research Hospital, Memphis, Tennessee, USA 38105. Email: Puneet.Bagga@stjude.org

Abstract

Purpose: Creatine-weighted CEST (CrCEST) MRI maps the recovery rate of creatine (T_{Cr}) in exercised muscle, reflecting mitochondrial oxidative phosphorylation (OXPHOS). However, its limited temporal resolution can cause discrepancies with T_{PCr} measurements 31P-MRS. This study introduces Fast-CrCEST, a novel method for reliable, high-temporal-resolution mapping of skeletal muscle OXPHOS.

Methods: Our proposed Fast-CrCEST method acquires Cr maps at a temporal resolution of 10s by applying RF saturation (B_1) at only ±1.8 ppm, in contrast to the conventional CrCEST protocol, which employs six frequency offsets and requires 30s per acquisition. Given that magnetization transfer ratio asymmetry (MTR_{asym}) depends on B_0 inhomogeneity, we modeled the pre-exercise MTR_{asym} for each muscle as a function of the corresponding B_0 inhomogeneity. This model was subsequently used to correct pixel-wise post-exercise B_0 shifts, allowing isolation of signal changes specifically associated with exercise-induced alterations in creatine levels. Seven subjects performed plantar flexion exercise at 3T, while CrCEST, fast-CrCEST, and 31P-MRS were performed. Recovery time constants in the gastrocnemius muscles, obtained from CrCEST (T_{Cr}) and fast-CrCEST (T_{fCr}), were compared with those derived from ^{31}P-MRS (T_{PCr}). To compare the accuracy of Cr recovery time constant measurements between CrCEST and fast-CrCEST, we performed simulations using 10s and 30s sampling intervals, incorporating experimentally measured noise levels.

Results: T_{fCr} showed a significant 1:1 correlation with T_{PCr} ($R^2 = 0.57$, $p = 0.048$), whereas T_{Cr} values were approximately three times higher than T_{PCr}, with a weaker correlation ($R^2=0.47$, $p=0.087$).

Conclusion: We present a novel method for correcting exercise-induced B_0 shifts in fast-CrCEST. This approach enables reliable assessment of post-exercise creatine recovery,

outperforming the conventional CrCEST protocol and demonstrating strong agreement with the gold-standard ^{31}P-MRS.

Keywords: CEST, Cr, PCr, skeletal muscle, OXPHOS

1 | INTRODUCTION

Mitochondrial oxidative phosphorylation (OXPHOS) is a critical metabolic pathway consisting of oxidation-reduction reactions that produce adenosine triphosphate (ATP), the primary energy currency required by skeletal muscles during exercise.[1] OXPHOS capacity varies significantly across populations, with endurance athletes exhibiting considerably greater mitochondrial oxidative capacity compared to sedentary lean or overweight individuals.[2] Conversely, compromised mitochondrial OXPHOS functionality is associated with various pathological conditions including muscular disorders, neurodegenerative diseases, aging, and cancer.[3-12] Such impairments often manifest clinically as exercise intolerance, severely impacting patient quality of life and physical capabilities.[13]

Currently, invasive muscle biopsies represent the gold-standard method to quantify mitochondrial OXPHOS capacity. However, biopsies have inherent limitations, including patient discomfort, risk of complications, and limited feasibility for repeated assessments over time. The gold standard technique, 31-Phosphorus magnetic resonance spectroscopy (31P-MRS) has traditionally been used to non-invasively quantify mitochondrial function.[14-18] Phosphocreatine (PCr) is hydrolyzed during muscle contraction to regenerate ATP from ADP, and subsequently resynthesized during recovery through the creatine kinase (CK) reaction, which biochemically couples PCr and creatine (Cr).[19,20]

$$\mathrm{PCr} + \mathrm{ADP} + \mathrm{H}^{+} \overset{\mathrm{CK}}{\Leftrightarrow} \mathrm{Cr} + \mathrm{ATP}$$

31P-MRS has been increasingly used to investigate mitochondrial dysfunction in aging and neurodegenerative disorders through alterations in high-energy phosphate metabolism.[15,21-23] However, the broader application of ^{31}P-MRS can be limited by its relatively low intrinsic sensitivity, the need for specialized hardware, and lower spatial resolution compared to proton-based imaging techniques.

Recently, creatine-weighted chemical exchange saturation transfer (CrCEST) MRI has emerged as a promising technique capable of mapping post-exercise Cr recovery kinetics with high sensitivity and spatial resolution using proton (1H) coils.[24-26] CrCEST MRI is performed by applying spectrally selective radio-frequency (RF) saturation pulses (B_1) at ±1.8 ppm to saturate the labile amine protons on Cr. Due to chemical exchange between the amine protons and bulk water, magnetization is transferred to water, resulting in a decrease in the water signal that is proportional to the free Cr concentration. The inherent B_0 inhomogeneity in a region of interest (ROI) leads to an inaccurate CrCEST contrast.[27] To correct for B_0 inhomogeneity, a partial z-spectrum at four additional offsets (±1.5 and ±2.1 ppm) is acquired (**Figure 1A**), leading to a longer acquisition time per time point.[27,28] A representative comparison between CrCEST with 31P-MRS is shown in **Figures 1B** and **1C**, adapted from DeBrosse et al.,[29] which demonstrates CrCEST overestimates Cr recovery time constant by approximately twofold compared to the gold standard PCr kinetics. Given that PCr recovery time constants can be as short as ~20s,[18,30] substantial portion of the Cr signal decline may occur within the first 30s window over which the first CrCEST data point is generally acquired (**Figure 1D**).[31] Thus, 30s temporal resolution of CrCEST may not accurately capture critical early recovery dynamics immediately following exercise.

In this study, we propose an advanced approach that we call "*Fast-CrCEST*". In Fast-CrCEST, we propose to increase the temporal resolution of acquisition by 3-fold by only acquiring two offsets (±1.8 ppm), compared to the typical 6 offsets used in conventional CrCEST. To correct for the inherent B_0 inhomogeneity, we propose a novel method for B_0 correction of the high temporal resolution CEST data. We compare the outcomes of conventional and Fast-CrCEST with the gold standard 31P-MRS. We demonstrate the practical utility of Fast-CrCEST in mapping skeletal muscle OXPHOS in healthy adult subjects, establishing its potential for clinical

translation as a reliable and non-invasive alternative for mitochondrial OXPHOS assessment in vivo.

2 | THEORY

The underlying principle of CEST MRI involves the selective saturation of solute-pool protons by RF irradiation at their specific resonance frequency.[32] The water signal S attenuates as the saturated solute-pool protons chemically exchange with bulk water protons. The CEST-spectrum or z-spectrum (Z) can be generated after applying RF irradiation at each frequency offset ($\Delta\omega_j$) prior to acquisition, where $j \in [-k,k]$ and k is the maximum offset index. Each distinct CEST proton pool manifests as a Lorentzian lineshape, $L(a_i,\sigma_i,\omega_i)$, characterized by its amplitude (a_i), line width (σ_i), and center frequency offset (ω_i). Mathematically, Z can be expressed as the sum of these Lorentzian lines, or equivalently as the sum of the sampled water signals ($S(\Delta\omega_j)$) at each ω_j (Equation 1):

$$Z = \sum_{i=1}^{N} L(a_i, \sigma_i, \omega_i) = \sum_{j=-k}^{+k} S(\Delta\omega_j) \tag{1}$$

where, N is the total number of CEST proton pools considered.

For skeletal muscle, the pre-exercise Z (Z_{pre}) is primarily influenced by the following CEST pools: (i) direct water proton saturation (DS), the largest water signal intensity drop occurring at 0 ppm (ω_{DS}), (ii) conventional semi-solid magnetization transfer (MT) arising from the "bound" pool of water molecular cross-relaxing with protons in the free water pool, (iii) amide proton transfer (APT) at 3.5ppm (ω_{APT}), arising from the exchangeable amide protons in the backbone of mobile proteins and peptides, (iv) exchange-relayed nuclear Overhauser effect (rNOE) at -3.5ppm (ω_{rNOE}), from aliphatic protons of mobile macromolecules, and (v) CrCEST at 1.8ppm (ω_{Cr}), from the exchangeable amine protons of Cr.

Hence,

$$Z_{pre} = L(DS_{pre}) + L(MT_{pre}) + L(APT_{pre}) + L(rNOE_{pre}) + L(CrCEST_{pre}) \tag{2}$$

At high B_1 (~3μT), typically used for CrCEST acquisitions, the contributions of APT and rNOE at ±1.8ppm are negligible.[29,33-35] Additionally, the asymmetry analysis of the Z (also called magnetization transfer ratio asymmetry, MTR_{asym}) can separate the symmetrical contribution of DS and MT. Therefore, RF irradiation at only two frequency offsets (±1.8 ppm) is sufficient to quantify the pre-exercise CrCEST effect using MTR_{asym} at +1.8ppm ($MTR_{asymPre}$), defined as the percentage difference between $S_{pre}(-1.8)$ and $S_{pre}(+1.8)$ (Equation 3):

$$\mathrm{MTR_{asymPre}} = \frac{\mathrm{S_{pre}}(-1.8) - \mathrm{S_{pre}}(+1.8)}{\mathrm{S_{pre}}(-1.8)} * 100 \tag{3}$$

However, as the resonance frequency in MRI is proportional to B_0, even a minor magnetic field inhomogeneity (ΔB_0) can cause substantial frequency shifts in Z.[27] Conventionally, retrospective ΔB_0 correction requires acquiring additional saturation offsets (±1.5 and ±2.1 ppm), followed by spline/Lorentzian interpolation of the Z, thereby limiting the CrCEST temporal resolution to ~30s (5s/saturation offset x 6 offsets).[27,28]

After an intervention such as mild plantar flexion exercise, the post-exercise Z (Z_{post}) and the associated MTR_{asym} ($MTR_{asymPost}$) are given by Equations 4a and 4b, respectively:

$$Z_{post} = L(DS_{post}) + L(MT_{post}) + L(APT_{post}) + L(rNOE_{post}) + L(CrCEST_{post}) \tag{4a}$$

$$\mathrm{MTR_{asymPost}} = \frac{\mathrm{S_{post}}(-1.8) - \mathrm{S_{post}}(+1.8)}{\mathrm{S_{post}}(-1.8)} * 100 \tag{4b}$$

The intramuscular pH remains relatively constant below 60% of maximal voluntary contraction (MVC) during plantar flexion,[36] and therefore does not influence the CEST contrast. Consequently, exercise-induced changes in Cr concentration, driven by the CK reaction, should be the primary contributor to $MTR_{asymPost}$. However, additional contribution to $MTR_{asymPost}$ arises from plantar flexion-induced motion, which perturbs B_0,[37] causing post-exercise ΔB_0 (ΔB_{0Post}) to deviate from the pre-exercise ΔB_0 (ΔB_{0Pre}), thereby necessitating further B_0 correction.

We propose constraining the CEST acquisition to two frequency offsets specific to Cr (±1.8 ppm), thereby reducing the temporal resolution to 10s (5s per offset x 2 offsets). To achieve this, we introduce a novel approach for correcting muscle-specific ΔB_0 as follows:

A quadratic function f is first fitted for each muscle to model the pre-exercise $MTR_{asymPre}$ to the corresponding ΔB_{0Pre} for all pixels i in a muscle having N_{muscle} pixels:[38]

$$MTR_{asymPre}=f(\Delta B_{0Pre}) \tag{5}$$

where, $\Delta B_{0Pre}=[\Delta B_{0Pre}(1), \Delta B_{0Pre}(2), \ldots, \Delta B_{0Pre}(i)]$, $MTR_{asymPre}=[MTR_{asymPre}(1), MTR_{asymPre}(2), \ldots, MTR_{asymPre}(i)]$, and $i \in [1, N_{muscle}]$.

Next, the same function f is applied to the post-exercise ΔB_{0Post} values at each pixel to estimate how much of the observed MTR_{asym} is explained by the post-exercise ΔB_{0Post} alone ($MTR_{asym\Delta B0}$) (Equation 6):

$$MTR_{asym\Delta B0}(i)=f(\Delta B_{0Post}(i)) \tag{6}$$

We hypothesize the measured $MTR_{asymPost}$ to be the combination of $MTR_{asym\Delta B0}$ and the MTR_{asym} caused by exercise-induced Cr change ($MTR_{asym\Delta Cr}$):

$$MTR_{asymPost}(i) = MTR_{asym\Delta B0}(i) + MTR_{asym\Delta Cr}(i) \tag{7}$$

Rearranging Equation 7 yields $MTR_{asym\Delta Cr}$ at each pixel i in a muscle (Equation 8):

$$MTR_{asym\Delta Cr}(i) = MTR_{asymPost}(i) - MTR_{asym\Delta B0}(i) \tag{8}$$

Next, for an entire muscle, $MTR_{asym\Delta Cr}$(muscle) can be calculated using Equation 9:

$$\mathrm{MTR}_{\mathrm{asym\Delta Cr}}\,(\mathrm{muscle}) = \frac{1}{\mathrm{N_{muscle}}}\sum_{\mathrm{i=1}}^{\mathrm{N_{muscle}}} \mathrm{MTR}_{\mathrm{asym\Delta Cr}}\,(\mathrm{i}) \tag{9}$$

3 | METHODS

3.1 | Study Design

The protocol was approved by the Institutional Review Board, with informed written consent obtained prior to the scan. Seven healthy adult participants (male: 5, mean age: 35.1±6.8 years) were scanned. Each participant underwent one MR acquisition for conventional CrCEST, Fast-CrCEST, and 31P-MRS spanning two one-hour sessions on different days on a 3T whole-body scanner (MAGNETOM Prisma, Siemens Healthcare, Erlangen, Germany). MVC was determined prior to scanning as the peak pressure that each participant could handle. During each of three acquisitions, each participant underwent mild plantar flexion exercise for 2 minutes at a constant rate of 45 flexions per minute inside the scanner using a MR compatible ergometer (Trispect, Ergospect GmbH, Innsbruck, Austria) with pedal pressure set to 8PSI (30-40% of MVC). The MRI protocols for each of the three different techniques, CrCEST, Fast-CrCEST, and 31P-MRS, are summarized in **Figure S1**.

3.2 | CrCEST MRI

Both conventional- and Fast-CrCEST data were acquired with a Tx/Rx 1/15-channel 1H knee coil (Siemens Medical Solutions, PA, USA). A localizer was first acquired on the right calf of each participant to center the imaging slice on the thickest part of the calf muscle. A baseline CrCEST protocol was run which included one image without selective saturation, B_0 map,[27] and four baseline CrCEST images.[26] The reference image without selective saturation was used to segment the lateral gastrocnemius (LG), medial gastrocnemius (MG) and soleus (Sol). Immediately following a 2-minute exercise, a recovery CrCEST protocol was run which included post-exercise CrCEST acquisitions (20 images at 30s temporal resolution for CrCEST, 63 images at 10s temporal resolution for Fast-CrCEST), B_0 map, and one image without selective saturation. Post-exercise muscle boundaries were delineated from post-exercise CrCEST images. Technical parameters for CrCEST and B_0 map acquisitions can be found in Chakraborty et al.[39] Briefly, CrCEST imaging parameters were set as follows: TR/TE=4.7/2.3 ms, slice thickness=10mm, flip angle=10°, B_{1rms}=3μT, in-plane resolution=1.25×1.25mm^2, matrix

size=128×128, field of view=160×160mm^2. CrCEST images were acquired within a frequency shift range of ±1.5, ±1.8, ±2.1 ppm relative to water resonance. For the proposed technique, Fast-CrCEST images were acquired at ±1.8 ppm relative to the water resonance and included two dummy scans.

3.3 | 31P-MRS

31P-MRS was performed with a 1H/31P dual-tuned flex transmit/receive surface coil of 11cm diameter (RAPID Biomedical GmbH, Würzburg-Rimpar, Germany) using an unlocalized free induction decay (FID) sequence: measurements=96, averages=2, bandwidth=5000Hz, and TR=5s. The sequence included 15 minutes of acquisition, with 5 min of baseline, 2 min of exercise and 8 min of post-exercise recovery. The temporal resolution of 31P-MRS was kept at 10s to match the temporal resolution of Fast-CrCEST acquisitions.

3.4 | Data analysis

All images and data/statistical analyses were performed using in-house MATLAB scripts. Figures 1B and 1C were extracted from images of a previous publication using a free online tool (www.graphreader.com).

3.4.1 | Conventional CrCEST

The LG, MG, and Sol muscles were manually segmented. MTR_{asym} was computed using Equations 3 and 4b, and then corrected for B_0 inhomogeneity to yield the post-exercise Cr-specific $MTR_{asym\Delta Cr}$ signal.[25,40] The Cr recovery time-constant (T_{Cr}) for each muscle was estimated using spline interpolation as the time required for the signal to decay by 63.2%.

3.4.2 | Fast-CrCEST

For Fast-CrCEST, the LG, MG, and Sol muscles were first manually segmented. The B_0-corrected $MTR_{asym\Delta Cr}$ signals, reflecting exercise-induced changes in Cr within the three

muscles, were calculated as described in Section 2. The Cr recovery time-constant (T_{fCr}) for each muscle was estimated by fitting a monoexponential decay model, given by:

$$\mathrm{MTR}_{\mathrm{asym\Delta Cr}}(t) = \mathrm{MTR}_{\mathrm{asym\Delta Cr}_{\mathrm{asymp}}} + \mathrm{MTR}_{\mathrm{asym\Delta Cr}_{\mathrm{amp}}} * e^{\left(-\frac{t}{T_{fCr}}\right)} \quad (10)$$

where, $\mathrm{MTR}_{\mathrm{asym\Delta Cr}_{\mathrm{asymp}}}$ is the asymptotic value, and $\mathrm{MTR}_{\mathrm{asym\Delta Cr}_{\mathrm{amp}}}$ is the amplitude of the exponential decay. Additionally, the pre-exercise B_0-corrected MTR_{asym} value for each muscle was calculated from the y-intercept of the function f in Equation 5.

3.4.3 | 31P-MRS

The 31P-MRS spectra were phased, baseline-corrected, and fitted with Lorentzians. The area under the curve of PCr peak ([PCr]) was quantified from each FID and normalized to the baseline value. Post-exercise [PCr] values were expressed as a percentage of the pre-exercise level. The PCr recovery time-constant, T_{PCr}, was estimated by fitting the data to a mono-exponential growth function:[41]

$$[\mathrm{PCr}](t) = [\mathrm{PCr}]_{\mathrm{initial}} + [\mathrm{PCr}]_{\mathrm{amp}} * \left(1 - e^{\left(-\frac{t}{T_{PCr}}\right)}\right) \quad (11)$$

where, $[PCr]_{initial}$ is the normalized [PCr] value at the first post-exercise time point, and $[PCr]_{amp}$ represents the amplitude of recovery.

3.4.4 Monte Carlo simulation of error estimation

To quantify the effect of sampling interval on the accuracy of T_{Cr} and T_{fCr} estimates, Monte Carlo simulations were performed. For each $\mathrm{MTR}_{\mathrm{asym\Delta Cr}_{\mathrm{amp}}}$ (4%, 8%, 12%, 16%) and for each ground-truth time-constant from 20s to 100s in 1s increments, an ideal mono-exponential recovery curve was generated. Gaussian noise with a standard deviation (SD) matching experimentally observed noise levels was simulated 100 times and added, yielding 100 data per condition. Specifically, for the 4% amplitude condition, the mean noise SD observed in the MG

was used to match experimentally observed MG recovery curves; for the remaining three amplitudes (8%, 12%, and 16%), the mean noise SD observed in the LG was used to reflect realistic LG recovery curves. Each data was sampled at 30s and 10s intervals corresponding to conventional- and Fast-CrCEST and refitted using Equation 10 to estimate T_{Cr} and T_{fCr}, respectively. Mean absolute errors were then calculated by comparing with the ground-truth values to evaluate performance differences between the two sampling intervals.

3.5 | Statistical Analysis

Simple linear regression analyses were performed to evaluate the relationships between T_{Cr} and T_{PCr}, and between T_{fCr} and T_{PCr}. Since the majority of the 31P-MRS signal acquired using a surface coil originates from the gastrocnemius muscle (~2.8cm depth for our coil),[25] the mean T_{Cr} and T_{PCr} value from the LG and MG were used for statistical comparison with T_{PCr}. The coefficient of determination (R^2) was calculated for the second-order polynomial fits evaluated between MTR_{asym} and ΔB_{0Pre} in LG, MG, and Sol. For Fast-CrCEST, the standard deviation (SD) of the noise after fitting Equation 10 and the 95% confidence intervals of the predicted parameters were calculated. A two-sided Student's t-test was used throughout the analysis, with $p<0.05$ considered statistically significant. A confidence interval (CI) was reported for all reported parameters derived from Fast-CrCEST analysis, and their mean and standard deviation were computed.

4 | RESULTS

The proposed Fast-CrCEST approach is illustrated in **Figure 2**. Panel A shows manual segmentation of the LG, MG, and Sol muscles on a baseline anatomical MRI of the calf. Panels B and C display the corresponding $MTR_{asymPre}$ and ΔB_{0Pre} maps, respectively. In panel D, a representative scatter plot of $MTR_{asymPre}$ versus ΔB_{0Pre} in the MG muscle is shown (orange crosses), along with the second-order polynomial fit (dotted black line) described by: $MTR_{asymPre} = -118*(\Delta B_{0Pre})^2 + 128*\Delta B_{0Pre} + 6.4$ ($R^2=0.996$, $p<0.001$). The B_0-corrected baseline

MTRasymPre value can be estimated by setting ΔB_{0Pre}=0 in this equation, yielding 6.4%. Panels E and F show the $MTR_{asymPost}$ at the first post-exercise time point (t=10s) and ΔB_{0Post} maps, respectively. In panel G, the $MTR_{asymPost}$ values (hollow circles) in MG are plotted against the corresponding ΔB_{0Post}. The black crosses represent the $MTR_{asym\Delta B0}$ values calculated using Equation 6, which model the expected MTR_{asym} arising solely from the change from ΔB_{0Pre} to ΔB_{0Post}. The vertical distance between each circle and its corresponding cross (difference between $MTR_{asymPost}$ and $MTR_{asym\Delta B0}$) represents the exercise-induced Cr-specific signal change ($MTR_{asym\Delta Cr}$) in MG. Scatter plots of $MTR_{asymPre}$ versus ΔB_{0Pre} and $MTR_{asymPost}$ versus ΔB_{0Post} for the LG, MG and Sol in the same subject are shown in **Figure S2**.

The B_0-corrected $MTR_{asym\Delta Cr}$ maps for the same subject, acquired using the Fast-CrCEST sequence with a 10s temporal resolution over a 10-minute post-exercise recovery period, are presented in **Figure 3**. Pixel intensity reflects the Cr-specific MTR_{asym} signal, with red indicating elevated values and blue indicating values approaching baseline. At 10s post-exercise, red pixels are prominent across the muscle regions, reflecting a marked increase in free Cr concentration. The maps show that red pixels gradually diminish over the first two minutes and transition to predominantly blue, consistent with Cr rephosphorylation to PCr through the creatine kinase reaction.

The post-exercise Cr recovery kinetics measured using CrCEST and Fast-CrCEST, along with the ground truth PCr recovery curve obtained from 31P-MRS in the same subject, are shown in **Figure 4**. Using conventional-CrCEST, the estimated T_{Cr} were 148s (LG), 102s (MG), and 108s (Sol). In contrast, T_{PCr} measured by 31P-MRS was 47s. With the Fast-CrCEST approach, T_{fCr} were 66s (LG), 45s (MG), and 50s (Sol), demonstrating closer agreement with the PCr kinetics.

Primary outcomes of the three MRI techniques for all subjects are summarized in **Table 1**. The 31P-MRS measured T_{PCr} was found to be 52±16s. The T_{Cr} values measured by conventional CrCEST in the three muscles were 203±99s (LG), 108±54s (MG), and 86±54s (Sol). The

corresponding T_{fCr} measured by Fast-CrCEST were 62±22s (LG), 78±29s (MG), and 55±73s (Sol). Secondary metrics related to Fast-CrCEST, such as B_0-corrrected $MTR_{asymPre}$, $\mathrm{MTR}_{\mathrm{asym\Delta Cr}_{\mathrm{amp}}}$, the standard deviation (SD) of residual noise after fitting Equation 10, and R^2 values of the predicted function f in Equation 5, are summarized in **Table S1**. The CIs of B_0-corrrected $MTR_{asymPre}$ values were very narrow for MG and Sol but were wider for LG. In contrast, the CIs of $\mathrm{MTR}_{\mathrm{asym\Delta Cr}_{\mathrm{amp}}}$ were consistently narrow across all three muscles. The R^2 values of the predicted function f in Equation 5 were consistently high in MG (0.98±0.01) and Sol(0.97±0.02), and moderate in LG (0.68±0.3), with five out of seven cases in LG exceeding 0.8.

The mean T_{fCr} in LG and MG showed a significant correlation with T_{PCr} (R^2=0.57, p=0.048, T_{Cr}=1.1*T_{PCr}+11.2), with a slope close to 1, indicating strong 1:1 correspondence **(Figure 5)**. In contrast, the mean T_{Cr} in LG and MG was not significantly correlated with T_{PCr} (R^2=0.47, p=0.087, T_{Cr}=2.9*T_{PCr}+3.8), and it overestimated the values by nearly threefold.

Figure 6 presents simulation results comparing Cr recovery kinetics and the accuracy of time constant estimation using conventional and Fast-CrCEST. Panels A-B depict the theoretical fraction of Cr remaining to be recovered, expressed as a percentage of the first post-exercise value, for two muscles with T_{Cr} values of 20s (panel A) and 50s (panel B), respectively. For T_{Cr}=20s (A), approximately 61% of Cr remains at 10s (the first Fast-CrCEST time point), dropping to 37% at 20 s and 22% at 30 s (the first conventional CrCEST time point). In contrast, for T_{Cr}=50 s (B), around 55% of Cr still remains at 30s. Panels C-F illustrates the error in estimating the time-constant using conventional CrCEST (red dots) and Fast-CrCEST (blue dots) across four synthetic datasets with different MTR_{asym} amplitudes and added Gaussian noise. The horizontal dashed line indicated a 10% error threshold. Fast-CrCEST maintained <10% error across all simulated time constants (except for a couple of points), including shorter T_{Cr} values (<30s) and always smaller errors than conventional CrCEST.**5 | DISCUSSION**

Our study introduces Fast-CrCEST, a novel method of acquiring CrCEST data that achieves threefold higher temporal resolution than the conventional sequence. By sampling only two frequency offsets at ±1.8ppm, Fast-CrCEST produces B_0-corrected Cr-specific MTR_{asym} images every 10s, compared with the 30s temporal resolution of the conventional six-offset acquisition (30s). This enhancement is critical because in healthy adults, the T_{PCr} can be as short as 20s,[18,30] meaning 63% of the post-exercise signal change occurs within that brief window. Given that PCr resynthesis is stoichiometrically coupled to a decrease in free Cr via the CK reaction, capturing these rapid dynamics demands sub-30s sampling. In our pilot cohort, T_{fCr} derived from Fast-CrCEST closely matched T_{Cr} measured by 31P-MRS, indicating that its 10s temporal resolution tracks Cr fluctuations accurately and yields a reliable estimate of the recovery time constant, a marker of mitochondrial OXPHOS capacity. Fast-CrCEST therefore complements 31P-MRS while overcoming the temporal limitation of conventional CrCEST, positioning it as a viable, non-invasive tool for quantifying skeletal-muscle energetics in a clinical setting.

We found that the first minute of post-exercise data acquisition is critical for accurately estimating the Cr recovery time constant. In healthy adults, PCr recovery follows mono-exponential kinetics with time-constants as short as 20s.[18,30] Our simulation for a muscle with T_{Cr}=20s indicates that a conventional CrCEST sequence with 30s temporal resolution captures only one data point as ~78% of Cr recovers. In contrast, for a muscle with higher T_{Cr}=50s, 54% of Cr still remains to recover at the 30s time point. These findings highlight the advantage of the 10s temporal resolution of Fast-CrCEST, which enables more detailed sampling of the steep early recovery phase and yields a more accurate estimate of T_{fCr}. This is supported by the significant correlation between T_{fCr} and gold-standard T_{PCr} obtained from 31P-MRS in our dataset, with a regression slope approaching 1. Monte Carlo simulations further demonstrated that Fast-CrCEST theoretically maintained mean T_{fCr} estimation errors below 10% for shorter recovery time-constants (<30s), even under more error-prone low $\mathrm{MTR}_{\mathrm{asym}\Delta\mathrm{Cr}_{\mathrm{amp}}}$ values,

further highlighting the advantage of higher temporal resolution. The regression slope of 2.9 between conventional CrCEST T_{Cr} and T_{PCr} observed in our dataset is consistent with findings reported by DeBrosse et al.[29] (mean T_{Cr}=84s versus mean T_{PCr}=46s in 14 healthy adults), confirming systematic overestimation of T_{Cr} by conventional CrCEST. This discrepancy likely arises from the inadequate sampling of the early post-exercise recovery phase, which Fast-CrCEST captures more effectively.

The percentage increase in amplitude of exercise-induced Cr-specific $MTR_{asymΔCr}$ showed an increase of 11.4±4% in LG, 6.8±1.4% in the MG, and 3.9±2.1% in the Sol between pre- and post-exercise, consistent with previously reported values in the literature.[31,39] The consistently small CIs in the estimation of $MTR_{asymPre}$ demonstrate that Fast-CrCEST provides a robust estimate of $\mathrm{MTR}_{\mathrm{asymΔCr}_{\mathrm{amp}}}$ in all three muscle groups. The pre-exercise $MTR_{asymPre}$ for each muscle group showed values of 15.5±9.4% in the LG, 6.9±0.8% in the MG, and 6.9±0.8% in the Sol. A necessary pre-condition for the reliability of these estimates is the availability of $ΔB_0$ values close to zero. In our data, the LG muscle exhibited markedly large CIs across subjects because $ΔB_0$ close to zero could never be achieved in that muscle, despite careful slice shimming. A representative case is shown in **Figure S2A**. By contrast, the $MTR_{asymPre}$ values for MG and Sol (range: 5.5-8.4%) were reliable for all subjects with narrow CIs, and fall within the range reported in the literature,[31,39] confirming that Fast-CrCEST can reliably quantify $MTR_{asymPre}$ when adequate $ΔB_0$ coverage is present.

This study has certain limitations. We used standard water-saturation shift-referencing (WASSR) to generate B_0 field inhomogeneity maps before and after exercise.[27] A core assumption of the proposed Fast-CrCEST framework is that the B_0 inhomogeneity remains generally stable during the post-exercise period, given that no motion takes place. However, gradual B_0 field drift may still occur due to heating of scanner components during gradient-intensive MR sequences over time, as observed in NOE experiments.[33,42] Similar local magnetic

field drifts are a well-recognized issue in functional MRI studies as well.[43] To mitigate such effects, an interleaved gradient echo-based B_0 mapping sequence can be implemented alongside the CEST acquisition to regress out the effect of such frequency drifts.[28] Additionally, while MTR_{asym} is relatively stable around the optimal RF power level,[44] B_1 inhomogeneity correction techniques can be used to correct for minor B_1 shifts.[45]

A second limitation of this study is that recovery kinetics for conventional CrCEST, Fast-CrCEST, and 31P-MRS were obtained from three separate scans performed over two days. Although care was taken to ensure that the exercise bouts across the three sets were identical, inter-session variability may still influence direct comparisons. A large-scale study is required to further confirm the robustness of these findings.

6 | CONCLUSION

Our study introduced “Fast-CrCEST”, an advanced technique that increases temporal resolution by threefold over the conventional CrCEST approach. We demonstrated its utility by mapping dynamic changes in skeletal muscle metabolism post-exercise in healthy participants and comparing it with the gold standard 31P-MRS technique thereby underlining its promise for clinical translation as a potential alternative for in vivo muscle mitochondrial OXPHOS assessment. Moreover, the underlying theory of Fast-CrCEST can be adapted to other CEST-based imaging applications, particularly in scenarios requiring high temporal resolution.

ACKNOWLEDGEMENTS

The authors thank Ms. Jennifer Vallet and Dr. Mitchell Taylor for their technical support and Ms. Pamela Adede for her assistance with participant recruitment.

DATA AVAILABILITY STATEMENT

Data will be made available upon request.

TABLES

Table 1: Recovery time constants of CrCEST and fast-CrCEST and 31P-MRS

Subject ID	31P-MRS	Conventional CrCEST			Fast-CrCEST		
	T_{PCr} (s)	T_{Cr} (s)			T_{fCr} (s)		
		LG	MG	Sol	LG	MG	Sol
1	50	270	209	95	70	95	87
2	83	365	116	40	88	112	15
3	32	88	55	160	19	35	5
4	41	132	84	140	71	77	202
5	47	148	102	108	66	45	50
6	53	261	126	36	62	112	16
7	60	158	65	22	60	68	12
Mean	52	203	108	86	62	78	55
SD	16	99	54	54	22	29	73

Figure Legends

Figure 1. Illustration of creatine-weighted chemical exchange saturation transfer (CrCEST) sequence. (A) Schematic of the B_1 saturation scheme used in CrCEST acquisition, with selective saturation applied at ±1.5, ±1.8, and ±2.1 ppm, applied in 5s blocks, resulting in a total acquisition time of 30s per point. (B-C) Representative mono-exponential recovery curves of Cr (B) and phosphocreatine (PCr, C) following exercise over time (t), respectively, acquired using CrCEST and 31P-MRS, respectively. Both datasets were adapted from Figures 1C and 1D of the DeBrosse et al.[29] Notably, the Cr recovery time constant (T_{Cr}) is more than 2x that of PCr. (D) Simulated Cr recovery curves based on known PCr dynamics demonstrate that a 30s temporal resolution may be insufficient to capture early recovery kinetics, particularly in short T_{Cr} cases (~20-40s), where substantial Cr signal decline can occur during the 30s window over which the first data point is acquired.

Figure 2. Demonstration of the fast- creatine-weighted chemical exchange saturation transfer (CrCEST) approach in a 37-year-old male participant. (A) Segmentation of the lateral gastrocnemius (LG), medial gastrocnemius (MG), and soleus (Sol) on an axial anatomical calf image. (B-C) Pre-exercise MTR_{asym} map acquired at +1.8 ppm and the corresponding B_0 inhomogeneity (ΔB_0) map derived from the water-saturation shift-referencing (WASSR) scan, both overlaid on the muscle masks. (D) Pixel-wise regression of MTR_{asym} with ΔB_0 in MG; the dotted line depicts the quadratic polynomial fit. (E-F) Post-exercise MTR_{asym} and ΔB_0 maps acquired after mild plantar-flexion exercise. (G) Scatterplot of post-exercise MTR_{asym} versus ΔB_0 in MG (circles). Black crosses indicate the expected value of MTR_{asym} due to change in B_0 assuming no change in creatine (Cr) concentration. Hence, the Cr-related change in MTR_{asym} can be quantified by subtracting the ΔB_0-induced component (i.e., the vertical distance between each circle and its corresponding cross).

Figure 3. B_0-corrected post-exercise $MTR_{asym\Delta Cr}$ maps acquired using fast- creatine-weighted chemical exchange saturation transfer (CrCEST) at a temporal resolution of 10s over a 10-minute post-exercise recovery period. Each frame depicts voxel-wise CrCEST asymmetry (%) at +1.8 ppm, corrected for B_0 inhomogeneity, in a representative axial slice of the lower leg encompassing the soleus (Sol), lateral gastrocnemius (LG), and medial gastrocnemius (MG) muscles. Elevated MTR_{asym} immediately following exercise (red pixels, time=10-60s) reflects increased free creatine concentration in the muscles, which gradually returns to baseline over time (blue pixels, time>120s). This spatially and temporally resolved mapping of dynamic changes in CrCEST signal reflects muscle-specific variations in mitochondrial oxidative phosphorylation capacity.

Figure 4. Comparison of post-exercise creatine (Cr) and phosphocreatine (PCr) recovery kinetics measured using three different techniques. (A) Creatine-weighted chemical exchange saturation transfer (CrCEST) recovery curves acquired with a conventional protocol (temporal resolution = 30s), showing mono-exponential decay in MTR_{asym} for the lateral gastrocnemius (LG), medial gastrocnemius (MG) and soleus (Sol) muscles. Estimated recovery time constants (T_{Cr}) were 148s (LG), 102s (MG), and 108s (Sol), respectively. (B) PCr recovery kinetics measured using non-localized 31P-MRS, showing mono-exponential post-exercise recovery with a time constant of 47s. (C) Fast-CrCEST recovery curves acquired with a 10s temporal resolution yielded T_{fCr} values of 66s (LG), 45s (MG), and 50s (Sol), demonstrating better alignment with 31P-MRS-derived PCr kinetics. The higher sampling frequency of fast-CrCEST enables capture of crucial early post-exercise signal dynamics, thereby improving the accuracy of kinetic modeling.

Figure 5. Regression analysis comparing creatine (Cr) recovery time measured using Cr-weighted chemical exchange saturation transfer (CrCEST) (T_{Cr}, blue circles) and fast-CrCEST (T_{fCr}, red squares) with the phosphocreatine (PCr) recovery time (T_{PCr}) determined using 31P-

MRS. A significant linear correlation was observed between T_{fCr} and T_{PCr} (p=0.048), with a regression slope of 1.1, indicating close agreement between the two measurements. In contrast, no significant correlation was found between T_{Cr} and T_{PCr} (p=0.087), with a regression slope close to 3, indicating an overestimation of Cr recovery times. Dashed ellipses represent 95% confidence regions for each technique.

Figure 6. Simulation illustrating the creatine recovery kinetics and associated estimation error for conventional and fast-CrCEST techniques (C-F). (A-B) Theoretical mono-exponential recovery curves showing the fraction of free creatine (Cr) remaining after exercise for two representative recovery time constants: (A) T_{Cr}=20s and (B) T_{Cr}=50s. The y-axis represents the percentage of the first post-exercise value (time, t=0s). Colored dots denote the Cr signal remaining at 10s (red), 20s (blue), and 30s (magenta). (C-F) Percentage error in estimating creatine recovery time constant calculated with conventional (T_{Cr}, red circles; 30s sampling) and fast-CrCEST (T_{fCr}, blue circles; 10s sampling) across simulated curves with four different amplitudes: (A) 4%, (B) 8%, (C) 12%, and (D) 16%. For each true T_{Cr} (x-axis, 20-100s), 100 mono-exponential decay curves were generated and contaminated with Gaussian noise scaled to match experimental conditions (standard deviation (SD): 0.6 in panel C, 1.0 in panels D-F). The horizontal dashed line indicates a 10% error threshold. The higher temporal resolution of fast-CrCEST sequence enables crucial tracking of early recovery kinetics and consistently maintains <10% error, even for short T_{Cr} <30s.

Figure 1.

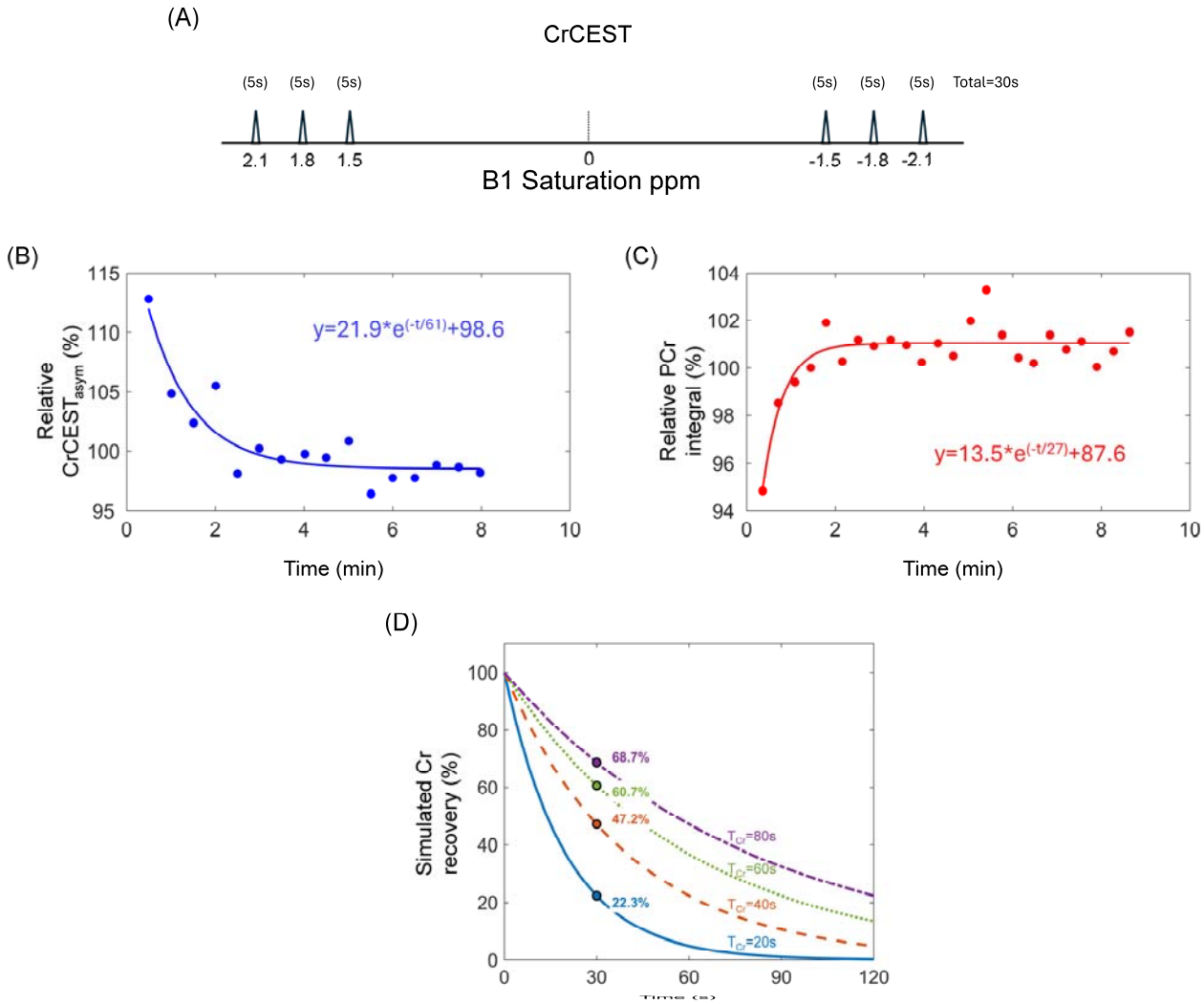
(A)
CrCEST
(5s) (5s) (5s)
(5s) (5s) (5s) Total=30s
2.1 1.8 1.5
0
-1.5 -1.8 -2.1
B1 Saturation ppm
(B)
y=21.9*e(-t/61)+98.6
Relative CrCESTasym (%)
Time (min)
(C)
y=13.5*e(-t/27)+87.6
Relative PCr integral (%)
Time (min)
(D)
68.7%
60.7%
47.2%
22.3%
TCr=80s
TCr=60s
TCr=40s
TCr=20s
Simulated Cr recovery (%)

Figure 2.

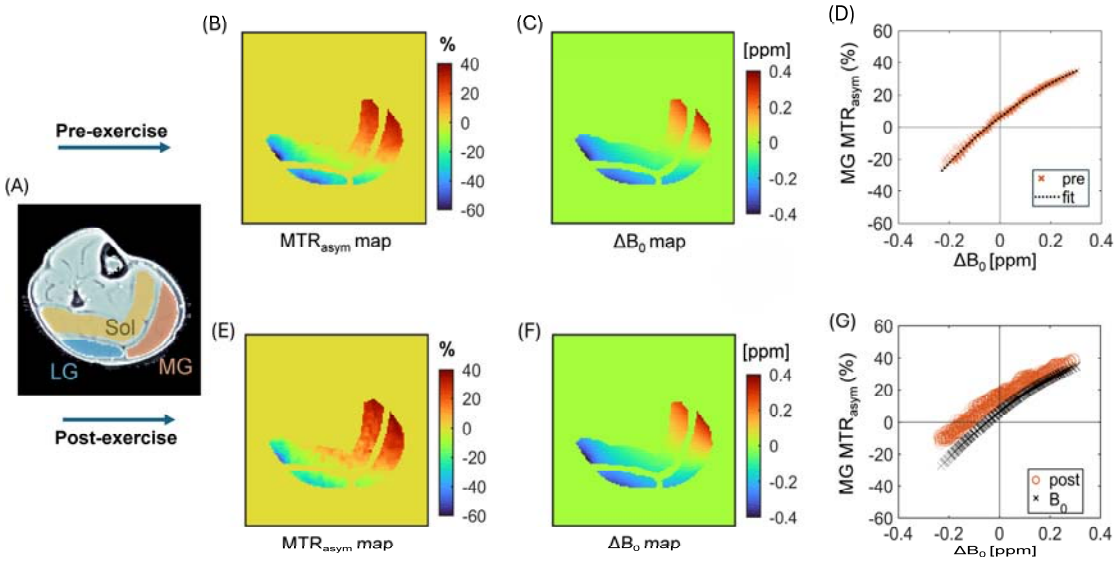

Figure 3.

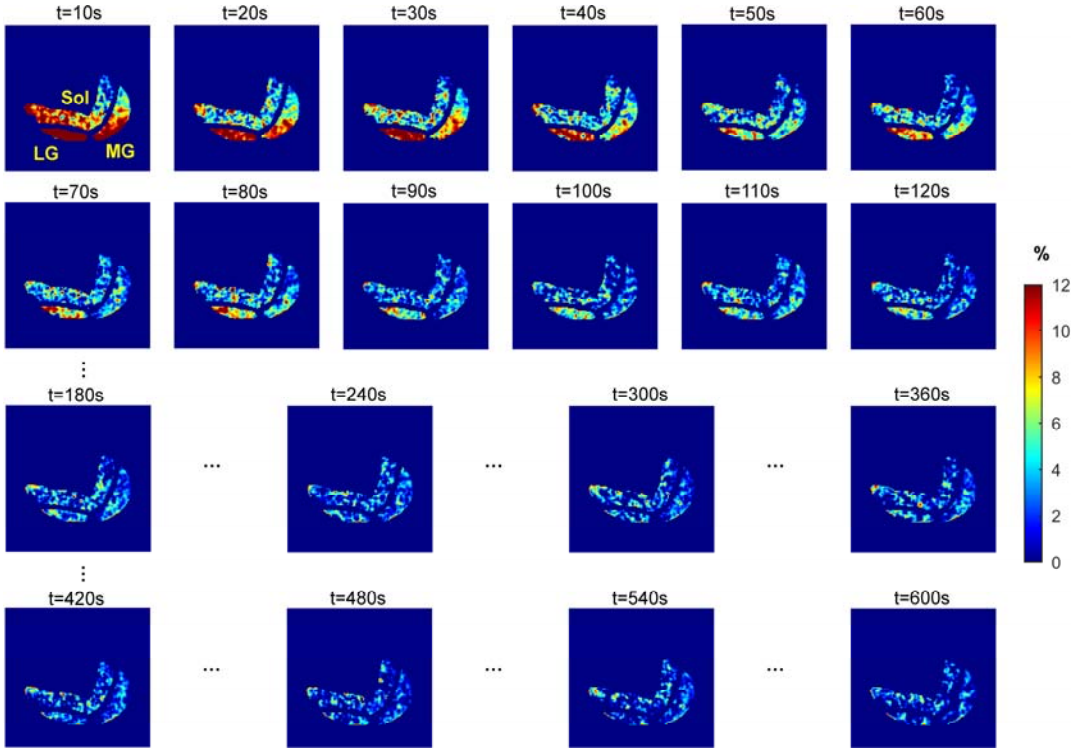

Figure 4.

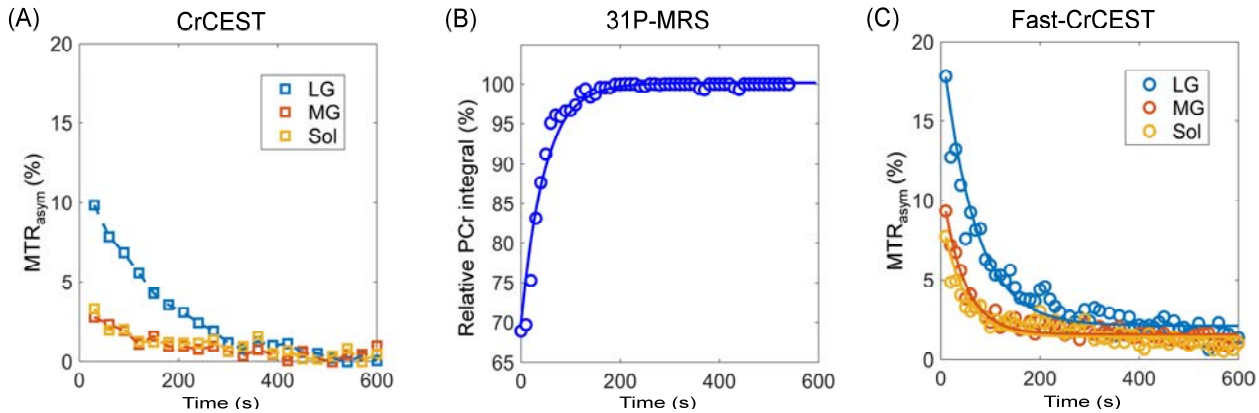

Figure 5.

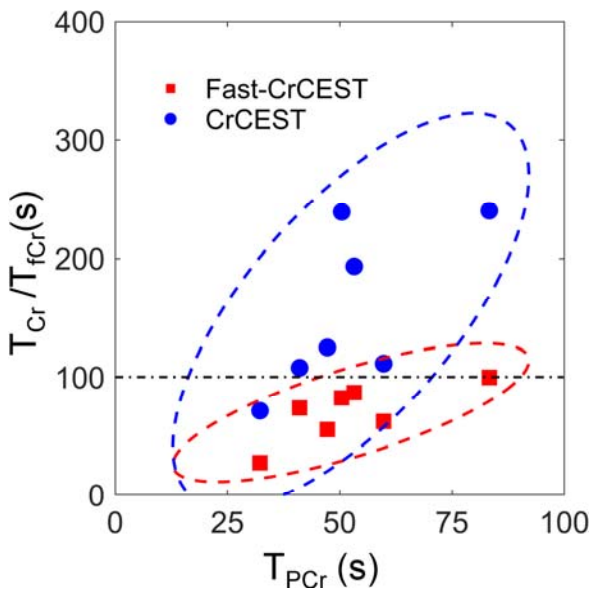

Figure 6.

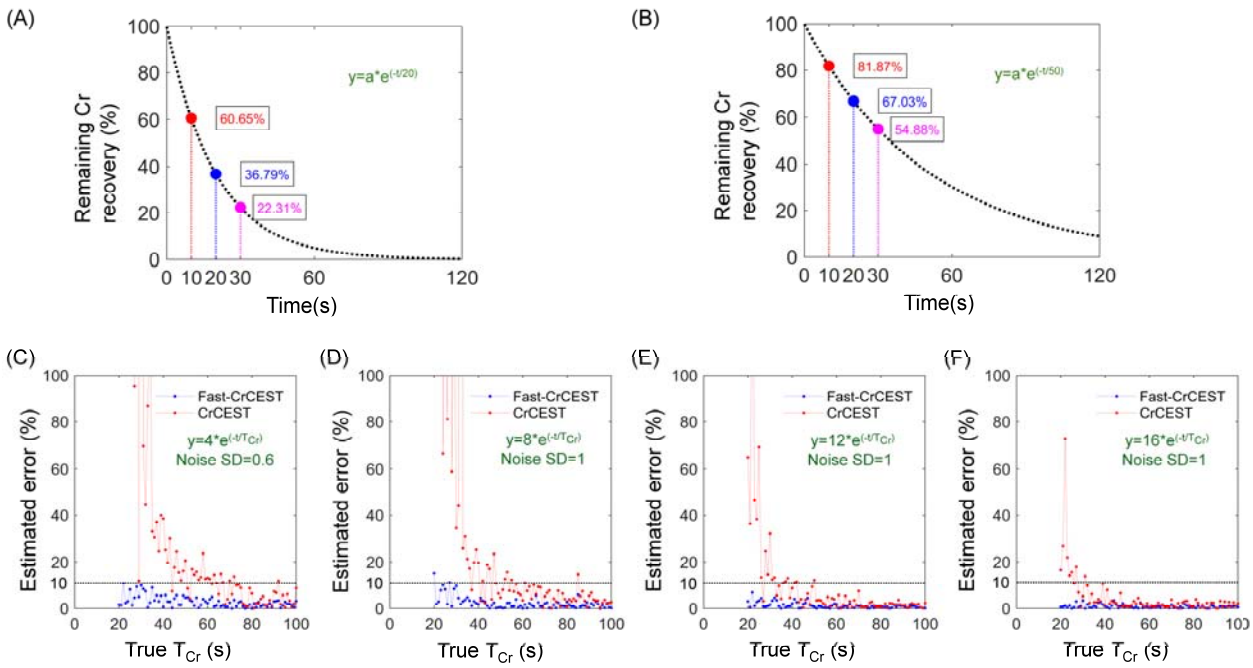
(A)
Remaining Cr recovery (%)
Time(s)
y=a*e(-t/20)
60.65%
36.79%
22.31%
(B)
Remaining Cr recovery (%)
Time(s)
y=a*e(-t/50)
81.87%
67.03%
54.88%
(C)
Estimated error (%)
True TCr (s)
Fast-CrCEST
CrCEST
y=4*e(-t/TCr)
Noise SD=0.6
(D)
Estimated error (%)
True TCr (s)
Fast-CrCEST
CrCEST
y=8*e(-t/TCr)
Noise SD=1
(E)
Estimated error (%)
True TCr (s)
Fast-CrCEST
CrCEST
y=12*e(-t/TCr)
Noise SD=1
(F)
Estimated error (%)
True TCr (s)
Fast-CrCEST
CrCEST
y=16*e(-t/TCr)
Noise SD=1

References

1. Deshpande OA, Mohiuddin SS. Biochemistry, Oxidative Phosphorylation. In: *StatPearls.* Treasure Island (FL) ineligible companies. Disclosure: Shamim Mohiuddin declares no relevant financial relationships with ineligible companies.2025.
2. Pesta D, Anadol-Schmitz E, Sarabhai T, et al. Determinants of increased muscle insulin sensitivity of exercise-trained versus sedentary normal weight and overweight individuals. *Sci Adv.* 2025;11(1):eadr8849.
3. Wallace DC. A mitochondrial bioenergetic etiology of disease. *J Clin Invest.* 2013;123(4):1405-1412.
4. Mancuso M, Angelini C, Bertini E, et al. Fatigue and exercise intolerance in mitochondrial diseases. Literature revision and experience of the Italian Network of mitochondrial diseases. *Neuromuscul Disord.* 2012;22 Suppl 3(3-3):S226-229.
5. Lodi R, Cooper JM, Bradley JL, et al. Deficit of in vivo mitochondrial ATP production in patients with Friedreich ataxia. *Proc Natl Acad Sci U S A.* 1999;96(20):11492-11495.
6. Schubert Baldo M, Vilarinho L. Molecular basis of Leigh syndrome: a current look. *Orphanet J Rare Dis.* 2020;15(1):31.
7. Kawamata H, Manfredi G. Proteinopathies and OXPHOS dysfunction in neurodegenerative diseases. *J Cell Biol.* 2017;216(12):3917-3929.
8. Migliavacca E, Tay SKH, Patel HP, et al. Mitochondrial oxidative capacity and NAD(+) biosynthesis are reduced in human sarcopenia across ethnicities. *Nat Commun.* 2019;10(1):5808.
9. Grandi FC, Astord S, Pezet S, et al. Characterization of SMA type II skeletal muscle from treated patients shows OXPHOS deficiency and denervation. *JCI Insight.* 2024;9(20).
10. Xu Y, Xue D, Bankhead A, 3rd, Neamati N. Why All the Fuss about Oxidative Phosphorylation (OXPHOS)? *J Med Chem.* 2020;63(23):14276-14307.
11. Gonzalez-Freire M, Scalzo P, D'Agostino J, et al. Skeletal muscle ex vivo mitochondrial respiration parallels decline in vivo oxidative capacity, cardiorespiratory fitness, and muscle strength: The Baltimore Longitudinal Study of Aging. *Aging Cell.* 2018;17(2).
12. Baran N, Lodi A, Dhungana Y, et al. Inhibition of mitochondrial complex I reverses NOTCH1-driven metabolic reprogramming in T-cell acute lymphoblastic leukemia. *Nat Commun.* 2022;13(1):2801.
13. Taivassalo T, Jensen TD, Kennaway N, DiMauro S, Vissing J, Haller RG. The spectrum of exercise tolerance in mitochondrial myopathies: a study of 40 patients. *Brain.* 2003;126(Pt 2):413-423.
14. Meyerspeer M, Boesch C, Cameron D, et al. (31) P magnetic resonance spectroscopy in skeletal muscle: Experts' consensus recommendations. *NMR Biomed.* 2020;34(5):e4246.
15. Kemp GJ, Ahmad RE, Nicolay K, Prompers JJ. Quantification of skeletal muscle mitochondrial function by 31P magnetic resonance spectroscopy techniques: a quantitative review. *Acta Physiol (Oxf).* 2015;213(1):107-144.
16. Meyer RA. A linear model of muscle respiration explains monoexponential phosphocreatine changes. *Am J Physiol.* 1988;254(4 Pt 1):C548-553.
17. Lanza IR, Bhagra S, Nair KS, Port JD. Measurement of human skeletal muscle oxidative capacity by 31P-MR spectroscopy: a cross-validation with in vitro measurements. *J Magn Reson Imaging.* 2011;34(5):1143-1150.
18. Lewsey SC, Weiss K, Schar M, et al. Exercise intolerance and rapid skeletal muscle energetic decline in human age-associated frailty. *JCI Insight.* 2020;5(20).
19. Hargreaves M, Spriet LL. Skeletal muscle energy metabolism during exercise. *Nat Metab.* 2020;2(9):817-828.

20. Walsh B, Tonkonogi M, Soderlund K, Hultman E, Saks V, Sahlin K. The role of phosphorylcreatine and creatine in the regulation of mitochondrial respiration in human skeletal muscle. *J Physiol.* 2001;537(Pt 3):971-978.
21. Jett S, Boneu C, Zarate C, et al. Systematic review of (31)P-magnetic resonance spectroscopy studies of brain high energy phosphates and membrane phospholipids in aging and Alzheimer's disease. *Front Aging Neurosci.* 2023;15:1183228.
22. Jing Y, Haeger A, Boumezbeur F, Binkofski F, Reetz K, Romanzetti S. Neuroenergetic alterations in neurodegenerative diseases: A systematic review and meta-analysis of in vivo(31)P-MRS studies. *Ageing Res Rev.* 2024;101:102488.
23. Sassani M, Alix JJ, McDermott CJ, et al. Magnetic resonance spectroscopy reveals mitochondrial dysfunction in amyotrophic lateral sclerosis. *Brain.* 2020;143(12):3603-3618.
24. Haris M, Nanga RP, Singh A, et al. Exchange rates of creatine kinase metabolites: feasibility of imaging creatine by chemical exchange saturation transfer MRI. *NMR Biomed.* 2012;25(11):1305-1309.
25. Kogan F, Haris M, Debrosse C, et al. In vivo chemical exchange saturation transfer imaging of creatine (CrCEST) in skeletal muscle at 3T. *J Magn Reson Imaging.* 2014;40(3):596-602.
26. Kogan F, Haris M, Singh A, et al. Method for high-resolution imaging of creatine in vivo using chemical exchange saturation transfer. *Magn Reson Med.* 2014;71(1):164-172.
27. Kim M, Gillen J, Landman BA, Zhou J, van Zijl PC. Water saturation shift referencing (WASSR) for chemical exchange saturation transfer (CEST) experiments. *Magn Reson Med.* 2009;61(6):1441-1450.
28. Poblador Rodriguez E, Moser P, Dymerska B, et al. A comparison of static and dynamic ΔB(0) mapping methods for correction of CEST MRI in the presence of temporal B(0) field variations. *Magn Reson Med.* 2019;82(2):633-646.
29. DeBrosse C, Nanga RPR, Wilson N, et al. Muscle oxidative phosphorylation quantitation using creatine chemical exchange saturation transfer (CrCEST) MRI in mitochondrial disorders. *JCI Insight.* 2016;1(18):e88207.
30. Menon RG, Xia D, Katz SD, Regatte RR. Dynamic (31)P-MRI and (31)P-MRS of lower leg muscles in heart failure patients. *Sci Rep.* 2021;11(1):7412.
31. Armbruster RR, Kumar D, Benyard B, et al. Personalized and muscle-specific OXPHOS measurement with integrated CrCEST MRI and proton MR spectroscopy. *Nat Commun.* 2024;15(1):5387.
32. Ward KM, Aletras AH, Balaban RS. A new class of contrast agents for MRI based on proton chemical exchange dependent saturation transfer (CEST). *J Magn Reson.* 2000;143(1):79-87.
33. Jones CK, Huang A, Xu J, et al. Nuclear Overhauser enhancement (NOE) imaging in the human brain at 7T. *Neuroimage.* 2013;77:114-124.
34. van Zijl PCM, Lam WW, Xu J, Knutsson L, Stanisz GJ. Magnetization Transfer Contrast and Chemical Exchange Saturation Transfer MRI. Features and analysis of the field-dependent saturation spectrum. *Neuroimage.* 2018;168:222-241.
35. Jin T, Wang P, Zong X, Kim SG. MR imaging of the amide-proton transfer effect and the pH-insensitive nuclear overhauser effect at 9.4 T. *Magn Reson Med.* 2013;69(3):760-770.
36. Homma T, Hamaoka T, Sako T, et al. Muscle oxidative metabolism accelerates with mild acidosis during incremental intermittent isometric plantar flexion exercise. *Dyn Med.* 2005;4(1):2.
37. Liu J, de Zwart JA, van Gelderen P, Murphy-Boesch J, Duyn JH. Effect of head motion on MRI B(0) field distribution. *Magn Reson Med.* 2018;80(6):2538-2548.

38. Sun PZ. Fast correction of B(0) field inhomogeneity for pH-specific magnetization transfer and relaxation normalized amide proton transfer imaging of acute ischemic stroke without Z-spectrum. *Magn Reson Med.* 2020;83(5):1688-1697.
39. Chakraborty K, Burman R, Nisar S, et al. Reliability of In Vivo Creatine-Weighted Chemical Exchange Saturation Transfer (CrCEST) MRI in Calf Skeletal Muscle of Healthy Volunteers at 3 T. *J Magn Reson Imaging.* 2024.
40. Wilson NE. ExerciseCEST. Zenodo. Published 2016. Accessed.
41. Forbes SC, Slade JM, Meyer RA. Short-term high-intensity interval training improves phosphocreatine recovery kinetics following moderate-intensity exercise in humans. *Appl Physiol Nutr Metab.* 2008;33(6):1124-1131.
42. Windschuh J, Zaiss M, Ehses P, Lee JS, Jerschow A, Regatte RR. Assessment of frequency drift on CEST MRI and dynamic correction: application to gagCEST at 7 T. *Magn Reson Med.* 2019;81(1):573-582.
43. Kopel R, Sladky R, Laub P, et al. No time for drifting: Comparing performance and applicability of signal detrending algorithms for real-time fMRI. *Neuroimage.* 2019;191:421-429.
44. Sun PZ, Zhou J, Huang J, van Zijl P. Simplified quantitative description of amide proton transfer (APT) imaging during acute ischemia. *Magn Reson Med.* 2007;57(2):405-410.
45. Windschuh J, Zaiss M, Meissner JE, et al. Correction of B1-inhomogeneities for relaxation-compensated CEST imaging at 7 T. *NMR Biomed.* 2015;28(5):529-537.